



Investigation of Nonlinear Electrokinetic and Rheological Behaviors of Typical Non-Newtonian Biofluids through Annular Microchannels

A. Hamed^{1,2}, M. Shams^{1,3†}, M. Charmiyan^{1,3} and E. Shirani⁴

¹ Department of Mechanical Engineering, Shiraz Branch, I.A.U., Shiraz, Iran

² Jabir-Ibn-Hayyan Institute of Higher Education, Rasht, Iran

³ Department of Mechanical Engineering, Isfahan University of Technology, Isfahan, 84156-83111, Iran

⁴ Foulad Institute of Technology, Fouladshahr, Isfahan, 84916-63763, Iran

†Corresponding Author Email: m.shams@me.iut.ac.ir

(Received October 12, 2014; accepted December 10, 2014)

ABSTRACT

Electroosmosis is the predominant mechanism for flow generation in lab-on-chip devices. Since most biofluids encountered in these devices reveal non-Newtonian behavior, a special understanding of the fundamental physics of the relevant transport phenomena seems vital for an accurate design of such miniaturized devices. In this study, a numerical analysis is presented to explore transport characteristics of typical non-Newtonian biofluids through annular microchannels under combined action of pressure and electrokinetic forces. The flow is considered steady and hydrodynamically fully developed. A finite difference method is used to solve the Poisson-Boltzmann and Cauchy momentum equations, while the classical boundary condition of no velocity-slip for the flow field is applied. The Poisson-Boltzmann equation is solved in the exact form without using the Debye-Hückel approximation. After numerically solving the governing equations, role of the key parameters in hydrodynamic behavior of the flow is analyzed and discussed.

Keywords: Annular microchannel; Non-Newtonian Biofluid flow; Electrokinetic and rheological behaviors; Numerical investigation

NOMENCLATURE

e	proton charge [C]	$TDMA$	tridiagonal matrix algorithm
E	electric field intensity [V m ⁻¹]		
f	friction factor	ΔR^*	dimensionless step size [-]
F	body force vector [N m ⁻³]	ε	relative dielectric constant [-]
k_B	boltzmann constant [J K ⁻¹]	ε_0	fluid permittivity [C V ⁻¹ m ⁻¹]
n	flow behavior index [-]	η	dimensionless Debye-Hückel parameter [-]
n_∞	ion density [m ⁻³]	λ_D	debye length [m]
p	pressure [Pa]	Λ	forcing ratio [-]
r	radial coordinate [m]	μ	effective viscosity [Pa s]
R	radius ratio [-]	μ_0	flow consistency constant [Pa s ⁿ]
Re	Reynolds number [-]	ρ	fluid density [kg m ⁻³]
R^*	dimensionless radial coordinate [-]	ρ_e	net electric charge density [C m ⁻³]
T_0	ambient temperature [K]	τ	shear stress [Pa]
u, v	axial/radial velocity component [ms ⁻¹]	ψ	electric potential [V]
u_{ref}	reference velocity [m s ⁻¹]	ψ^*	dimensionless electric potential [-]
U^*	dimensionless axial velocity [-]	ζ	dimensionless wall zeta potential [-]
V	velocity vector [m/s]		
x	axial coordinate [m]		

z_0	valence number of ions in the solution	ζ	wall zeta potential [V]
<i>EDL</i>	electric double layer	i/o	inner/outer cylinder
<i>EOF</i>	electroosmotic flow	m	mean
<i>PDF</i>	pressure driven flow	w	wall
<i>PDEOF</i>	combined pressure driven and electroosmotic flow	P	previous iteration
		Υ	Υ th grid node

1. INTRODUCTION

Recently, because of the rapid development in micro-fabrication technology, transport phenomena at micro-scale have attracted much attention, especially in the area of Micro-Electro-Mechanical-Systems (MEMS). Meanwhile, the concept of electroosmotic flow (EOF) is considered to be an inseparable part of many scientific and engineering applications, used for pumping, separating, and mixing in MEMS devices. Electroosmosis refers to the bulk liquid motion induced by an applied external electric field along electro-statically charged surfaces. An important characteristic of the electroosmosis-based microfluidic systems is that they do not require any moving components. This, in turn, results in a simpler design, an easier fabrication and more importantly, enhanced functionality for such systems compared to other mechanical-based configurations (Karniadakis *et al.* 2005; Probstein 1994).

In many practical applications, a compound electroosmotic and pressure driven force may be involved. However, hydrodynamic characteristics of combined pressure-driven and electroosmotic flow (PDEOF) differ significantly from those of both conventional pressure-driven flow (PDF) and pure electroosmotic flow (EOF).

Microfluidic devices, however, are more frequently involved in analyzing and/or processing biofluids (such as solutions of blood, saliva, protein and DNA), polymeric solutions and colloidal suspensions. These fluids reveal non-Newtonian characteristics and their behaviors are rather more complicated when compared with their Newtonian counterparts. For such fluids, both the fluid rheological behavior and the microscale effects are absolutely important and influential. Moreover, in order to describe the flow features of these flows, the more general Cauchy momentum equation with appropriate fluid constitutive relations must be used instead of the Navier-Stokes equations. Since electrokinetics results from the coupling of hydrodynamics and electrostatics, it is straightforward to believe that non-Newtonian hydrodynamics would modify the conventional Newtonian electrokinetics. Among various models proposed as fluid constitutive relations for non-Newtonian fluid flow behavior are power-law, Bingham, Eyring, PTT, and FENE-P models.

Most of the available research on non-Newtonian liquid flow in microchannels with consideration of electroosmotic forces is devoted to pure EOFs (e.g., see Zhao *et al.* 2008; Tang *et al.* 2009; Vasu

and De 2010; Zhao and Yang 2011; Ng and Qi 2013; Huang and Yao 2014), and there are only a handful number of studies targeting hydrodynamic aspects of the PDEOF counterparts in the literature. Berli and Olivares (2008), for example, theoretically obtained solutions for predicting the flow rate and electric current of non-Newtonian fluids as functions of simultaneously applied electric potential and pressure gradients in slit and cylindrical microchannels. Employing a finite volume method, Park and Lee (2008) numerically obtained flow field solution of full Phan-Thien-Tanner (PTT) constitutive equation in a rectangular duct under the action of an external electric field and an applied pressure gradient. Solving the Poisson-Boltzmann and the momentum equations using a finite difference method, Bharti *et al.* (2009) investigated electroviscous effects on steady, fully developed, pressure-driven flow of power-law liquids through a uniform cylindrical microchannel. They found that compared to the Newtonian liquids, the electroviscous effect is stronger in shear-thinning and weaker in shear-thickening liquids. Afonso *et al.* (2009, 2011) developed analytical solutions for hydrodynamic characteristics of combined electroosmotic and pressure driven flow of viscoelastic fluids in microchannels. Using a finite volume method, Davidson *et al.* (2010) numerically investigated electroviscous effects on pressure-driven flow of a Carreau shear-thinning liquid in a typical contraction-expansion microsystem at low Reynolds numbers. Hadigol *et al.* (2011) numerically analyzed PDEOF of power-law fluids in microchannels and micropumps using a finite volume scheme. Babaie *et al.* (2011) studied the electroosmotic flow of power-law fluids in the presence of pressure gradient in a slit microchannel. Afonso *et al.* (2012) used a finite volume method to solve the relevant coupled equations for general electro-osmotic flows of viscoelastic fluids in a cross-slot geometry using the upper-convected Maxwell and the simplified Phan-Thien-Tanner models. Ng (2013) developed analytical solutions for steady EOF of a viscoplastic material, namely Casson fluid, through a parallel-plate microchannel. Most recently, Zhu *et al.* (2014) have discussed the periodical flow of power-law fluids with electroviscous effects through a rectangular microchannel. In this study, the time evolution of velocity field is computed for different types of fluids, periodical Reynolds number, zeta potentials and dimensionless electrokinetic width.

In many lab-on-chip systems, the cross section of microchannels made by modern micromachining

technology is close to an annular shape. Micro-annulus is a widely applicable form of microchannels used in the design and fabrication process of many practical micro technologies such as micro-heat pipes, -heat exchangers, -mixers, and micro-reactors (Nouri-Borujerdi and Layeghi 2005; Westheimer and “Bud” Peterson 2001; Scampavia *et al.* 1995; Kuznetsov *et al.* 2009). In practice, EOF in a capillary annulus is encountered in applications such as electrophoretic separation of proteins and chemical remediation of contaminated soil. In addition, the annulus geometry is also employed as a novel microfluidic model for blending chemical and biological fluids (Jian *et al.* 2010). However, in studying hydrodynamic features of the PDEOF of non-Newtonian fluids, the annular geometry has received much less attention compared with microchannels with other types of cross-section.

In the present paper, however, an original attempt has been made to scrutinize special hydrodynamic features of PDEOF of a typical biofluid through micro-annuli. A common rheological model for biofluids with shear-dependent viscosity, namely, the power-law model is employed in this study, since it represents adequately, for engineering purposes, the rheology of many biofluidic substances over a wide range of shear rates. Although this model does not asymptote to Newtonian behavior in the limits of both zero and very large shear rates, it has the advantage of both applicability and simplicity to justify its use in investigations of shear-dependent flow behaviors (Bharti *et al.* 2009). For instance, the dependence of blood viscosity on the shear rate or the non-Newtonian nature of blood may be described by the power-law model. This model can then be considered as a scientific basis for the study of blood fluidity in different disease conditions (Hussain *et al.* 1999). The governing nonlinear equations in the present study are treated numerically in the exact form without using the Debye-Hückel linearization, which allows the solution to cover flows with a wide range of electric potential values. In the following, after numerically solving the governing equations, role of the key parameters in hydrodynamic behavior of the flow is analyzed and discussed in detail.

2. MATHEMATICAL FORMULATION

A schematic diagram of the problem under consideration is shown in Fig. 1. The configuration consists of two concentric cylinders of inner and outer radii, r_i and r_o , respectively. It is assumed that the fluid passing through the micro-annulus obeys the power-law model and the flow is laminar and hydrodynamically fully developed. Moreover, the electrostatic potentials at the wall-fluid interfaces are ζ_i and ζ_o , as illustrated in the figure. Here, just a half channel is considered due to the symmetry through the horizontal mid-plane of the micro-annulus.

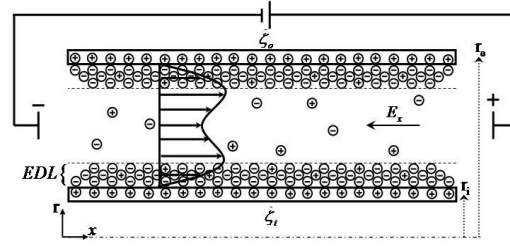


Fig. 1. Schematic diagram of the configuration in case of flow with adverse pressure gradient ($dp/dx > 0$).

2.1 Electric Potential Field

Assuming a symmetrical electrolyte of valence and a Boltzmann distribution of electrolyte ions in the electric double layer, the electric potential field is governed by the following Poisson equation

$$\nabla^2 \psi(r) = \frac{1}{r} \frac{d}{dr} \left(r \frac{d\psi}{dr} \right) = -\frac{\rho_e(r)}{\varepsilon \varepsilon_0} \quad (1)$$

where ψ is the electric potential, ε is the relative dielectric constant of the solution, ε_0 is the permittivity of a vacuum, and $\rho_e(r)$ is the net charge density at a radial distance r given by

$$\rho_e(r) = -2n_\infty z_0 e \sinh \left(\frac{z_0 e \psi}{k_B T_0} \right) \quad (2)$$

Here, n_∞ is the ion density, e is the proton charge, z_0 is the valence number of ions in the solution, k_B is the Boltzmann constant, and T_0 is the ambient temperature. A combination of Eqs. (1) and (2) gives

$$\frac{1}{r} \frac{d}{dr} \left(r \frac{d\psi}{dr} \right) = \frac{2n_\infty z_0 e}{\varepsilon \varepsilon_0} \sinh \left(\frac{z_0 e \psi}{k_B T_0} \right) \quad (3)$$

Non-dimensionalization of the above Poisson-Boltzmann equation yields

$$\frac{1}{R^*} \frac{d}{dR^*} \left(R^* \frac{d\psi^*}{dR^*} \right) = \eta^2 \sinh(\psi^*) \quad (4)$$

in which $\psi^* = z_0 e \psi / k_B T_0$, $R^* = r / r_o$, $\eta = k r_o$, and the parameter k known as the reciprocal of Debye length, λ_D , is given by

$$k = \left(2n_\infty z_0^2 e^2 / \varepsilon \varepsilon_0 k_B T_0 \right)^{1/2}.$$

On the system boundaries, however, we have set

$$\psi^*(R) = \zeta_i, \quad \psi^*(1) = \zeta_o \quad (5)$$

where $R = r_i / r_o$ and $\zeta_\alpha = z_o e \zeta_\alpha / k_B T_o$ ($\alpha = i, o$).

2.2 Flow Field

The Cauchy momentum equation governing the motion of the power-law electrolyte can be described as

$$\rho \frac{DV}{Dt} = -\nabla p + \nabla \cdot \tau + F \quad (6)$$

where ρ is the density, V denotes the velocity vector, p is the pressure, τ represents the stress tensor, and F is the body force vector. Assuming that the body force acts in the x direction, this term can be replaced with $\rho_e(r)E_x$, where $\rho_e(r)$ represents the local net charge density, and E_x is the external electric field intensity applied along the axis direction. To ensure that the flow is fully-developed, it is assumed that $L \gg l$, where L is the microchannel length and l is the length of the hydrodynamic developing (entry) region (Yang *et al.* 2005; Kandlikar *et al.* 2014).

The shear stress for power-law fluids follows the below consecutive relation

$$\tau_{rx} = \mu \frac{du}{dr} \quad (7)$$

In this relation, $u = u(r)$ is the axial velocity component for the steady-state and hydrodynamically fully developed flow considered here, while the transverse velocity component v equals zero. In addition, μ is the effective viscosity given by the following relation (Zhao *et al.* 2008; Bharti *et al.* 2009)

$$\mu = \mu_0 \left[\left(\frac{du}{dr} \right)^2 \right]^{\frac{n-1}{2}} \quad (8)$$

where μ_0 is the flow consistency constant and n is the flow behavior index. Depending on the value of n , different flow types such as shear-thinning flow (for $n < 1$) or shear-thickening flow (for $n > 1$) are encountered, and by setting $n = 1$ the Newtonian behavior is recovered.

Considering the already mentioned assumptions and combining Eqs. (2) and (6)-(8), the streamwise momentum equation is reduced to

$$\frac{\mu_0}{r} \frac{d}{dr} \left\{ r \left[\left(\frac{du}{dr} \right)^2 \right]^{\frac{n-1}{2}} \frac{du}{dr} \right\} = \frac{dp}{dx} + 2n_x z_o e E_x \sinh \left(\frac{z_o e \psi}{k_B T_o} \right) \quad (9)$$

Expressing the above equation in a dimensionless

form, we have

$$\frac{1}{R^*} \frac{d}{dR^*} \left\{ R^* \left[\left(\frac{dU^*}{dR^*} \right)^2 \right]^{\frac{n-1}{2}} \frac{dU^*}{dR^*} \right\} = \frac{r_o^{n+1}}{\mu_0 u_{HS}^n} \frac{dp}{dx} + \frac{r_o^{n+1}}{\mu_0 u_{HS}^n} 2n_x z_o e E_x \sinh(\psi^*) \quad (10)$$

where $U^* = u/u_{HS}$, and u_{HS} represents the Helmholtz-Smoluchowski electroosmotic velocity for power-law fluids given by Zhao *et al.* (2008)

$$u_{HS} = n \lambda_D^{\frac{n-1}{n}} \left(\frac{-\epsilon \epsilon_0 \zeta_o E_x}{\mu_0} \right)^{\frac{1}{n}} \quad (11)$$

Rewriting Eq. (10) using a new parameter Λ , we will obtain

$$\frac{1}{R^*} \frac{d}{dR^*} \left\{ R^* \left[\left(\frac{dU^*}{dR^*} \right)^2 \right]^{\frac{n-1}{2}} \frac{dU^*}{dR^*} \right\} = - \left(\frac{n+1}{n} \right)^n \Lambda - \frac{\eta^{n+1}}{n^n \zeta_o} \sinh(\psi^*) \quad (12)$$

in which ζ_o is the dimensionless form of ζ_o , and the forcing ratio, Λ , is defined as

$$\Lambda = \frac{u_{PD}^n}{u_{HS}^n} \quad (13)$$

Here, u_{PD} is a finite velocity whose value is related to the maximum velocity, U_{max} , of a pressure driven power-law flow in a microannulus (with $r_i \rightarrow 0$) as

$$u_{PD}^n = 2U_{max}^n = - \frac{r_o^{n+1}}{\mu_0} \left(\frac{n}{n+1} \right)^n \frac{dp}{dx} \quad (14)$$

After rearranging Eq. (12), the following equation can be readily obtained

$$n \Pi(R^*) \left[\frac{d^2 U^*}{dR^{*2}} + \frac{1}{nR^*} \left(\frac{dU^*}{dR^*} \right) \right] = - \left(\frac{n+1}{n} \right)^n \Lambda - \frac{\eta^{n+1}}{n^n \zeta_o} \sinh(\psi^*) \quad (15)$$

for which we have introduced

$$\Pi(R^*) = \left[\left(\frac{dU^*}{dR^*} \right)^2 \right]^{\frac{n-1}{2}} \quad (16)$$

Meticulously going through Eqs. (13)-(15), one can realize that for a positive u_{HS} , positive values of

Λ correspond to the case of pressure assisted flow ($dp/dx < 0$), while negative values of this quantity are associated with the pressure opposed flow ($dp/dx > 0$) and ultimately, $\Lambda = 0$ refers to the pure electroosmotic flow. The boundary condition for the velocity field is set as

$$U^*(R) = 0 \quad , \quad U^*(1) = 0 \quad (17)$$

3. SOLUTION PROCEDURE

Discretization of the governing equations based on an implicit finite difference method with a central difference scheme yields

$$\left(1 + \frac{\Delta R^*}{2R_Y^*}\right)\psi_{Y+1}^* - 2\psi_Y^* + \left(1 - \frac{\Delta R^*}{2R_Y^*}\right)\psi_{Y-1}^* = \eta^2 (\Delta R^*)^2 \sinh(\psi_Y^*) \quad (18)$$

$$n \Pi_Y \left\{ \left(1 + \frac{\Delta R^*}{2nR_Y^*}\right)U_{Y+1}^* - 2U_Y^* + \left(1 - \frac{\Delta R^*}{2nR_Y^*}\right)U_{Y-1}^* \right\} = (\Delta R^*)^2 \left[-\left(\frac{n+1}{n}\right)^n \Lambda - \frac{\eta^{n+1}}{n^n \zeta_o} \sinh(\psi_Y^*) \right] \quad (19)$$

where the subscript Y represents Y -th node in the one-dimensional grid considered here. To simplify the solution process and also to supply a better convergence, the following assumptions are made in the numerical simulation. In order to obtain a linear system of equations, the term Π in the left-hand side of Eq. (19) is replaced by the corresponding value of the previous iteration, say Π^P . This means that this term is considered as a constant at each iteration and hence, this quantity can be transferred to the right hand side of the discrete equation. Furthermore, it is observed that treating the term $\sinh(\psi^*)$ in Eq. (18) as a source term leads to the instability of the solution. Therefore, this term has been shifted to the left-hand side of this equation. According to the above, the resulting forms of the discrete equations are

$$\left(1 + \frac{\Delta R^*}{2R_Y^*}\right)\psi_{Y+1}^* - \left(2 + \eta^2 (\Delta R^*)^2 \Phi_Y^P\right)\psi_Y^* + \left(1 - \frac{\Delta R^*}{2R_Y^*}\right)\psi_{Y-1}^* = 0 \quad (20)$$

$$\left(1 + \frac{\Delta R^*}{2nR_Y^*}\right)U_{Y+1}^* - 2U_Y^* + \left(1 - \frac{\Delta R^*}{2nR_Y^*}\right)U_{Y-1}^* = \frac{(\Delta R^*)^2}{n \Pi_Y^P} \left[-\left(\frac{n+1}{n}\right)^n \Lambda - \frac{\eta^{n+1}}{n^n \zeta_o} \sinh(\psi_Y^*) \right] \quad (21)$$

where $\Phi_Y = \sinh(\psi_Y^*)/\psi_Y^*$, and the superscript P is used to show that the corresponding quantity is

calculated based on the value of the major variables at the previous iteration. After providing initial guess values for both equations, the discrete algebraic equations are solved by employing the Tridiagonal matrix algorithm (TDMA) scheme. Furthermore, the values of the quantities Π_Y and Φ_Y at each iteration are set as guess values for the next iteration. This procedure continues until the convergence criterion, which is the achievement of relative error of 10^{-8} , is satisfied. It is worth mentioning that although the step size $\Delta R^* = 0.001$ provided us with acceptable results in most cases, 15,000 grid points are used in the simulation to improve the accuracy and to obtain mesh independent results.

4. OTHER ASSOCIATED QUANTITIES

To this end, the main features of the problem under consideration have been presented and the numerical strategy used to solve the governing equations is discussed. After determining the velocity distribution, other associated hydrodynamic quantities such as friction factor, mean velocity, and viscosity ratio can be easily determined.

The friction factor is defined as

$$f_j = \frac{2\tau_{wj}}{\rho u_{HS}^2} \quad (22)$$

in which τ_w is the shear stress at the interface and $j = (i, o)$ represents the inner and outer walls, respectively. This factor can be expressed in the form of the Poiseuille number as follows

$$f_j \text{Re} = 2 \left[\left(\frac{dU^*(R_j)}{dR^*} \right)^2 \right]^{\frac{n}{2}} \quad (23)$$

where $R_j = \begin{cases} R & j = i \\ 1 & j = o \end{cases}$ and the Reynolds number

is specified as $\text{Re} = \rho u_{HS}^{(2-n)} r_o^n / \mu_o$.

The dimensionless mean velocity can be obtained through

$$U_m^* = \frac{2 \int_0^1 U^* R^* dR^*}{1 - R^{*2}} \quad (24)$$

It should be noted that in order to evaluate the value of the integral observed in the right-hand side of the above equation the trapezoidal rule is employed.

Another important parameter is the ratio of the viscosity at a given point to its value at the outer wall, namely the viscosity ratio, introduced as

$$\frac{\mu}{\mu_o} = \frac{\Pi(R^*)}{\Pi(1)} \quad (25)$$

5. RESULTS AND DISCUSSION

The main parameters governing fluid flow in fully developed combined pressure and electroosmotically driven flows in the annular microchannel considered here are found to be the radius ratio, R , dimensionless wall zeta potential, ζ , Debye-Hückel parameter, η , forcing ratio, Λ , and the flow behavior index, n . In the following, the interactive effects of the above mentioned influential parameters on major quantities such as the velocity distribution, Poiseuille number, fluid viscosity ratio and dimensionless mean velocity are discussed.

5.1 Velocity Distribution

Figure 2 shows a comparison between transverse distribution of the dimensionless velocity obtained through the current numerical investigation and the analytical solution presented in Tsao (2000) for pure electroosmotic Newtonian flow through a micro-annulus. Note here that since the analytical approach is based on the Debye-Hückel approximation, in the discrete equations we have set $\sinh(\psi^*) \cong \psi^*$ to

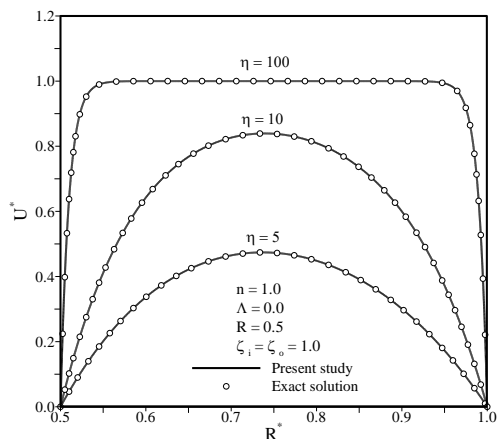


Fig. 2. Normalized velocity distribution versus radial distance: comparison of the results obtained in the present study with the exact solution given by Tsao (2000).

make a reasonable comparison. As seen, there is an excellent agreement between our results and those of Tsao (2000) at both low and high values of the Debye-Hückel parameter.

Figure 3 aims at elucidating the effect of the dimensionless zeta potential on the velocity field. This figure which is associated with the pressure assisted shear-thinning flow with $n = 0.5$, $\Lambda = 1$ and $\eta = 100$ reveals that as ζ approaches higher values, the maximum value of the velocity increases. As seen, at low values of the dimensionless zeta potential (i.e., $\zeta = 0.5$) the simplified solution under the Debye-Hückel approximation seems appropriate. Another noteworthy point is that at high values of the Debye-

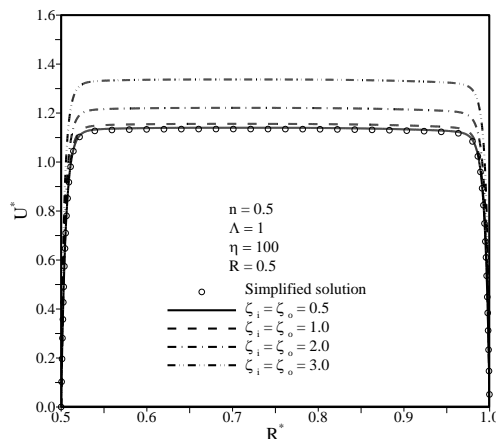


Fig. 3. Normalized velocity distribution across the channel at different values of ζ for the shear-thinning flow with $n = 0.5$ in case of the pressure assisted flow, while the simplified solution is related to $\zeta = 0.5$.

Hückel parameter (such as $\eta = 100$) the electric double layer is limited to a small region in the vicinity of the walls and a vast majority of the channel width is outside the electric double layer (EDL).

Presented in Fig. 4a are the dimensionless velocity distribution across the channel predicted by the current study and the analytical solution given by Tsao (2000), at different values of Λ and for $n = 0.5$, $\eta = 20$ and $\zeta_i = \zeta_o = 3$. One can readily infer from the figure that the simplifying assumption of the Debye-Hückel approximation seriously affects the flow field solution and leads to significant discrepancies between the numerical and analytical results not only for the pressure assisted flow, but also for the pure electroosmotic and pressure opposed flows. Furthermore, as expected, higher velocities exist in case of pressure assisted flow compared to the other flow patterns due to the cooperation of pure electroosmotic and Poiseuille flows in determining the final solution for the flow field while a favorable pressure gradient is applied. Interestingly, in case of pure electroosmotic flow with $n = 0.5$, the results show that the maximum velocity exceeds the Helmholtz-Smoluchowski velocity. It, however, is beyond the capability of the analytical solution to capture this phenomenon. To also consider the case with walls of arbitrary zeta potential, the effect of the ratio of zeta potentials, $\zeta_r (= \zeta_o / \zeta_i)$, on the velocity distribution for the shear-thinning and shear-thickening flows with $\eta = 10.0$ and $\Lambda = 5.0$ is demonstrated in Fig. 4b. It is observed that an increase in the value of ζ_r - which corresponds to increased values of the zeta potential at the outer wall, ζ_o , when ζ_i is set to 0.1- results in higher/lower amounts of velocity and consequently, greater/smaller mean velocity at the channel cross-section for the shear-thinning/shear-thickening flow pattern. The difference in the trends observed for the two flow patterns is due to the

diverse impact of the dimensionless zeta potential at the outer wall on the velocity distribution through Eq. (12) for different values of the flow behavior index.

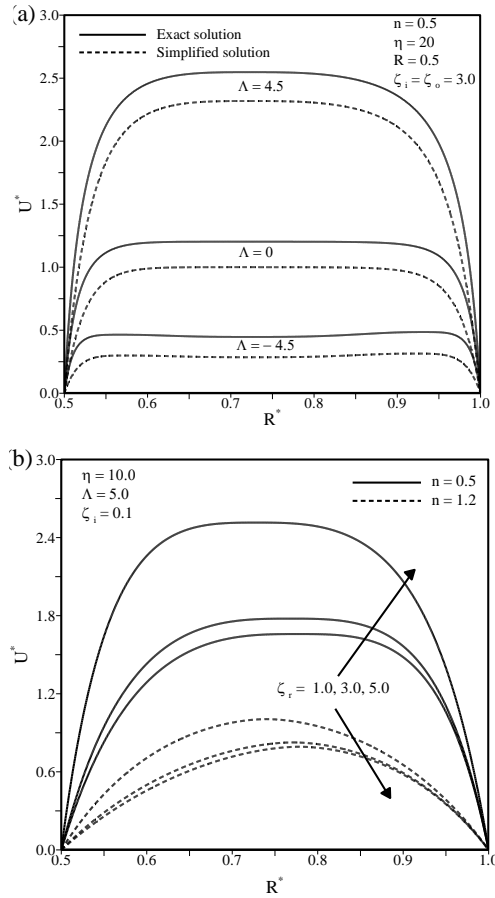


Fig. 4. Velocity profile across the channel at different values of (a) Λ (b) ζ_r .

Figure 5 illustrates normalized velocity distribution across the channel at different values of n and ζ for both pressure assisted and pressure opposed flows with $\eta=40$. Figure 5a states that for a positive value of the forcing ratio like $\Lambda=5$, the velocity profile pertained to the shear-thinning fluid exceeds its shear-thickening counterpart. This difference in velocity magnitude originates from the effect of n on the effective viscosity in Eq. (8). Furthermore, the shear-thinning flow is found to be more sensitive to the dimensionless zeta potential parameter, which shows that such a flow is absolutely prone to miscalculation of associated flow field quantities while applying the Debye-Hückel approximation. Similar to the pressure assisted flow, for the pressure opposed flow, the

effect of ζ on the shear-thinning flow is more pronounced, which is depicted in Fig. 5b. As is obvious from this figure, opposite contributions of the

pressure and electroosmotic forces to the fluid motion in this case bring about a velocity distribution with both a local minimum value at

moderate radial distances and sharp gradients in the vicinity of the system boundaries inherited from the pure electroosmotic and Poiseuille flows. Furthermore, just like the flow with favorable pressure gradient, in case of flow with adverse pressure gradient, increasing the dimensionless zeta potential increases the velocity for the shear-thinning flow, while the opposite is true for the shear-thickening flow throughout much of the channel cross section.

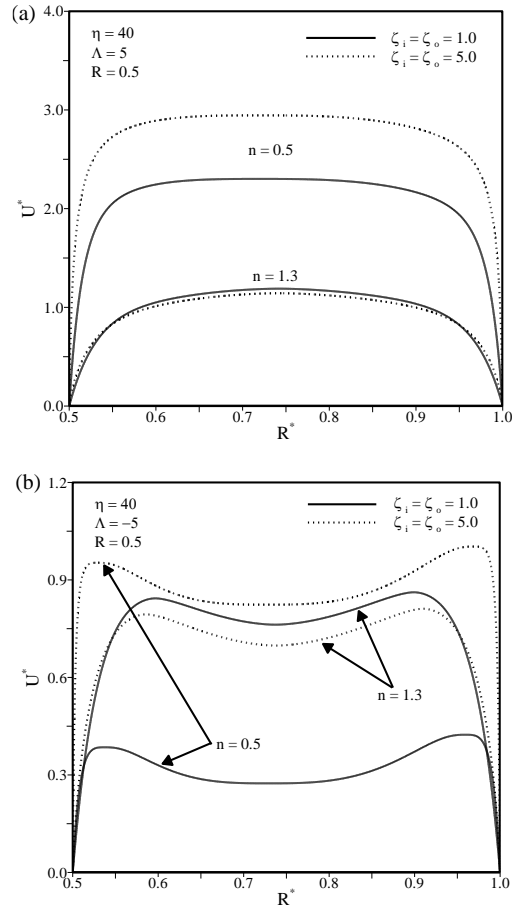


Fig. 5. Normalized velocity distribution across the channel at different values of n and ζ for (a) pressure assisted flow (b) pressure opposed flow.

5.2 Fluid Viscosity Ratio and Poiseuille Number

The fluid viscosity ratio versus the radial distance at different values of the flow behavior index for pressure assisted flow with $\eta=10$, $\Lambda=5$ and $\zeta_i = \zeta_o = 1$ is plotted in Fig. 6. It can be deduced

from the figure that for the shear-thinning flow a singularity occurs in the associated profiles due to the definition of the fluid viscosity ratio in Eq. (25). In addition, the shear-thickening fluids exhibit inviscid characteristics at special values of the radial distance where the viscosity ratio becomes zero. These observations, however, are related to the unrealistic physical results, introduced by the

power-law correlation, that viscosity either vanishes or becomes infinite in the limits of large or small shear-rates, respectively. Before the singularity point the viscosity increases with increasing the radial distance, while after the singularity the behavior is vice versa. Note that the singularities take place at the radial distances where the velocity gradient equals zero. For a Newtonian fluid, the viscosity remains constant across the channel, as expected. The behavior of the viscosity ratio associated with the shear-thickening fluids completely differs from that of the shear-thinning fluids so that this quantity exhibits a

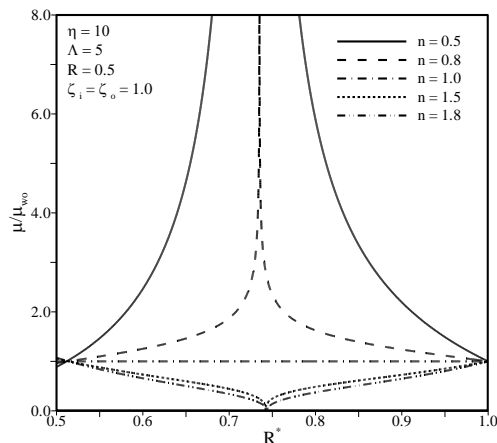


Fig. 6. Effect of the flow behavior index on the viscosity ratio for flow with $\eta = 10$, $\Lambda = 5$ and $\zeta_i = \zeta_o = 1$.

decreasing-increasing trend from the inner wall up to the outer boundary.

Figure 7 examines the effect of the Debye-Hückel parameter on the distribution of the viscosity ratio for the pressure assisted shear-thickening flow with $n = 1.2$, $\Lambda = 5$ and $\zeta_i = \zeta_o = 1$. It is observed that small values of η generate more monotonous viscosity distributions, while large values of this parameter cause sharp viscosity variations near the walls. In fact, at small values of η the velocity profile is nearly similar to that for the Poiseuille flow and a nearly uniform driving force exists in the flow domain. By increasing the dimensionless Debye-Hückel parameter, as stated before, EDL becomes limited to smaller regions close to the walls, restricting the electroosmotic driving force to smaller portions of the

flow. This, in turn, results in more plug-like velocity profiles and consequently, high velocity gradients inside the electric double layer as well as a sharp viscosity rise in the vicinity of the solid boundaries.

The Poiseuille number, which is considered as a crucial variable especially for optimization objectives, is discussed in the following. The inner and outer Poiseuille numbers as functions of R at different values of n and Λ for flow with $\eta = 5$ and $\zeta_i = \zeta_o = 1$ are demonstrated in Fig. 8. As is clear, the behaviors of the Poiseuille numbers at the

inner and outer walls are almost similar; i.e., at fixed values of the flow behavior index and the forcing ratio, both $f_i Re$ and $f_o Re$ decrease with increasing the radius ratio. In addition, at a fixed value of Λ , higher values of Poiseuille number are observed for the shear-thickening flow compared to the shear-thinning counterpart. It is also inferred from the figure that the pressure assisted flow exhibits greater values of shear stress than the pressure opposed flow; however, the discrepancy tends to diminish as the annular space becomes smaller (R increases). This observation

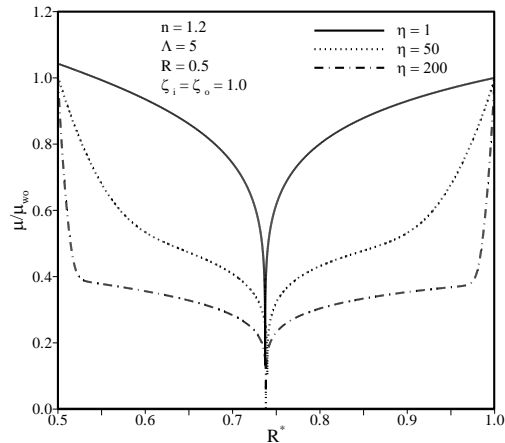


Fig. 7. Effect of the Debye-Hückel parameter on the viscosity ratio for the pressure assisted shear-thickening flow with $n = 1.2$, $\Lambda = 5$ and $\zeta_i = \zeta_o = 1$.

may be explained regarding the fact that the former flow pattern obtains higher velocity magnitudes and consequently greater velocity gradients inside the electric double layer.

Figure 9 is the exhibition of the Poiseuille number at the inner wall versus the Debye-Hückel parameter for different values of the wall zeta potential and flow behavior index, while the forcing ratio is fixed at $\Lambda = 5$. It can be stated that increasing both ζ and η monotonously increases the magnitude of $f_i Re$, regardless of the value of n . The reason is that an increase in the value of the former parameter leads to the production of greater electroosmotic driving forces within the domain, while enhancing the latter causes a reduction in the Debye length. Both of the aforementioned attitudes bring about larger velocity gradients inside EDL and consequently, greater Poiseuille numbers are achieved. In addition, considering similar behaviors of the Poiseuille numbers related to flows with $\Lambda = 0.5$ and $\Lambda = 5$ (not shown here), the conclusion made while comparing $f_i Re$ for the shear-thinning and shear-thickening flows in Fig. 8 is shown to apply not only to the special case of $\eta = 5$, but to the whole range of the Debye-Hückel parameter considered here. Another interesting point is that at lower values of η for which the effect of the electroosmotic force is dominant in wider portions

of the microchannel, the discrepancy between the Poiseuille number associated with the shear-thinning and shear-thickening flows becomes negligible.

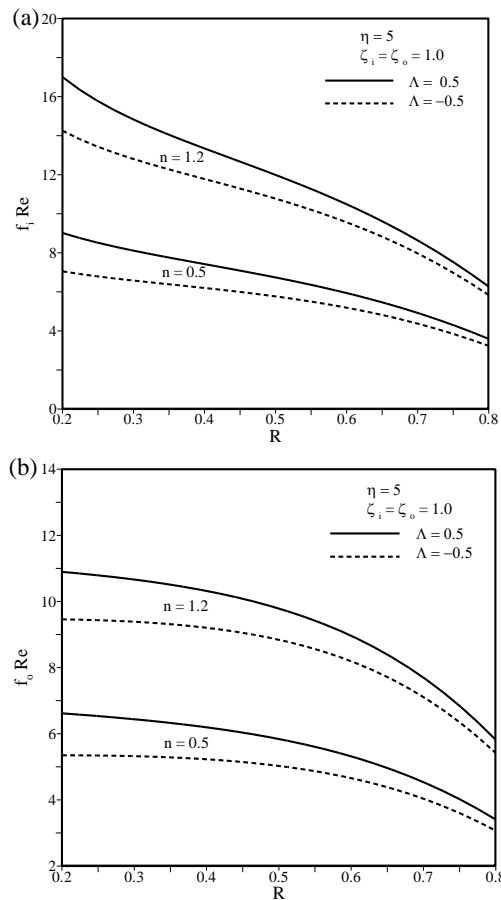


Fig. 8. Variation of the Poiseuille number with n and Λ in terms of R for flow with $\eta = 5$ and $\zeta_i = \zeta_o = 1$: (a) inner wall (b) outer wall.

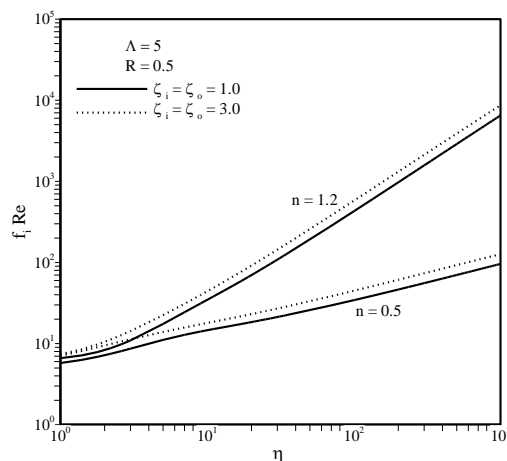


Fig.9. Variation of the Poiseuille number at the inner wall with n and ζ in terms of η for flow with $\Lambda = 5$ and $R = 0.5$.

5.3 Dimensionless Mean Velocity

The variation of the dimensionless mean velocity,

U_m^* -which can be considered as a measure for the volumetric flow rate- with n and Λ as a function of R is displayed in Fig. 10. Here, we have set $\eta = 5$ and $\zeta_i = \zeta_o = 1$. Generally speaking, for both shear-thinning and shear-thickening flows, higher dimensionless mean velocities are encountered while applying the favorable pressure gradient. However, for both fluids, the difference between the velocities pertained to the pressure assisted and pressure opposed flows becomes nearly undistinguishable at higher values of the radius ratio. In addition, regardless of the value of Λ , at lower values of R the mean velocity associated with the shear-thinning flow is greater than that of the shear-thickening flow, while at higher values of the parameter it is vice versa. Another noteworthy feature is that for all values of the flow behavior index and forcing ratio considered here, increasing values of R lead to a decrease in the dimensionless mean velocity.

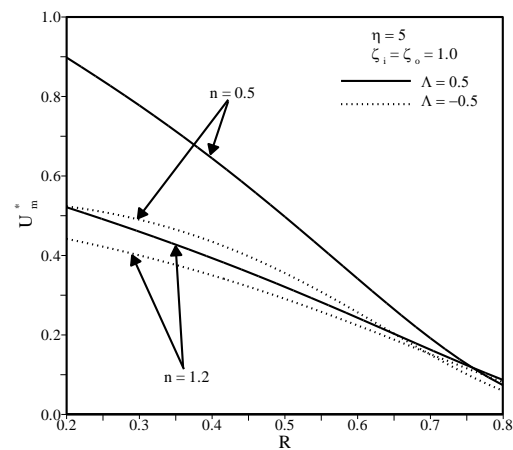


Fig.10. Variation of the dimensionless mean velocity with n and Λ in terms of the radius ratio for flow with $\eta = 5$ and $\zeta_i = \zeta_o = 1$.

Figure 11 is an illustration of the dimensionless mean velocity as a function of the Debye-Hückel parameter at different values of the dimensionless wall zeta potential and flow behavior index in case of pressure assisted flow with $\Lambda = 5$. Different behaviors are observed for the shear-thinning and shear-thickening flows. More precisely, U_m^* monotonously increases with an increase in η in case of shear-thickening flow, whereas a local maximum is observed in the profile related to the shear-thinning flow. Moreover, increasing values of the dimensionless zeta potential are found to drastically increase the mean velocity associated with the shear-thinning flow, while that of the shear-thickening flow is independent of ζ in a wide range of the Debye-Hückel parameter. This figure also suggests that for all values of the Debye-Hückel parameter presented here, higher volumetric flow rates would be attained by choosing a shear-thinning liquid as the working fluid.

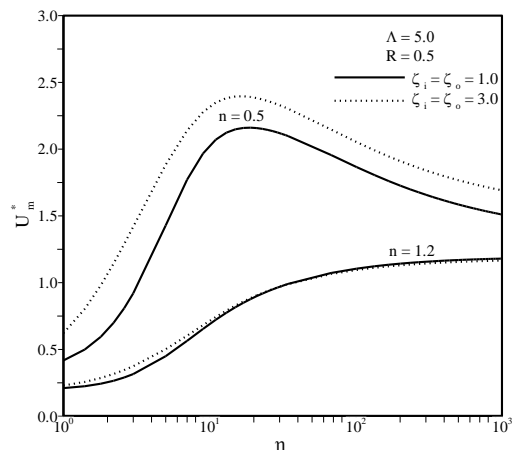


Fig. 11. Normalized mean velocity versus the Debye-Hückel parameter at different values of n and ζ in case of flow with favorable pressure gradient.

The dimensionless mean velocity versus the flow behavior index for the pressure assisted, pure electroosmotic and pressure opposed flows with $\eta = 10$ and $\zeta_i = \zeta_o = 1$ is plotted in Fig. 12. Inclusively going through the figure, one can readily deduce that increasing values of the flow behavior index tend to monotonously reduce the mean velocity for pressure assisted and pure electroosmotic flows, while exhibit a different trend in the presence of remarkable values of opposed pressure. To elucidate more, in case of pressure opposed flows, U_m^* firstly increases as n approaches higher values and after that, a decreasing trend is observed. It is instructive to mention that at higher values of the flow behavior index less sensitivity to the applied pressure gradient is observed. The evidence is the closeness of the mean velocity profiles for the shear-thickening flow. Moreover, for the parameters mentioned here, the highest value of the volumetric flow rate belongs to the pressure assisted shear-thinning flow with $n = 0.5$.

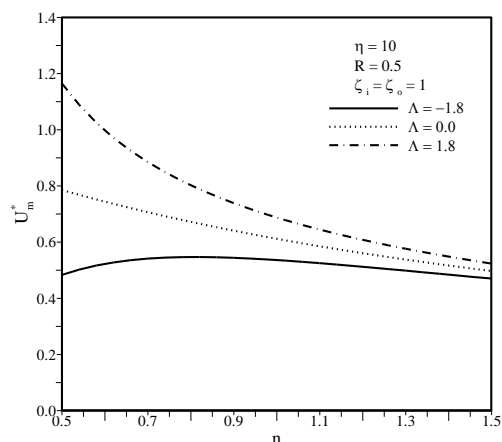


Fig. 12. Normalized mean velocity versus the flow behavior index for pressure opposed, pure electroosmotic and pressure assisted flows.

6. CONCLUSIONS

In the present study, the hydrodynamically fully developed combined pressure and electroosmotically driven flow of non-Newtonian power-law liquids through a uniform micro-annulus is investigated numerically. The Poisson-Boltzmann and Cauchy momentum equations are solved under the classical boundary condition of no velocity-slip for the flow field. Considering the Poisson-Boltzmann equation in the exact form without using the Debye-Hückel approximation, an iterative numerical scheme based on a finite difference method has been employed to solve the governing equations. The main influential parameters are found to be the radius ratio, R , flow behavior index, n , forcing ratio, Λ , dimensionless wall zeta potential, ζ , and the Debye-Hückel parameter, η . Some key results of this study can be summarized as follows:

- As ζ approaches higher values, the maximum value of the velocity increases. Furthermore, at high values of the Debye-Hückel parameter the electric double layer is limited to a small region in the vicinity of the walls and a vast majority of the channel width is outside the EDL.
- For the shear-thinning flows, a singularity occurs in the profiles due to the definition of the fluid viscosity ratio. Before the singularity point, the viscosity increases with increasing the radial distance, while after the singularity, the behavior is vice versa. The singularities take place at the radial distances where the velocity gradient equals zero. For a Newtonian fluid, however, the viscosity remains constant across the channel, as expected. The behavior of the viscosity ratio associated with the shear-thickening flows completely differs from that of the shear-thinning fluids so that this quantity exhibits a decreasing-increasing trend from the inner wall up to the outer boundary.
- The Poiseuille number is observed to increase with increasing values of the dimensionless Debye-Hückel parameter, the wall zeta potential and the flow behavior index, whereas it is a reducing function of the radius ratio.
- Increasing values of the flow behavior index tend to monotonously reduce the mean velocity for pressure assisted and pure electroosmotic flows, while exhibit a different trend in the presence of remarkable values of opposed pressure. To elucidate more, in case of pressure opposed flows, U_m^* firstly increases as n approaches higher values and after that, a decreasing trend is observed. Another noteworthy feature is that for all values of the flow behavior index and forcing ratio considered here, increasing values of R decrease the dimensionless mean velocity.

REFERENCES

Afonso, A. M., M. A. Alves and F. T. Pinho (2009).

- Analytical solution of mixed electroosmotic/pressure driven flows of viscoelastic fluids in microchannels. *Journal of Non-Newtonian Fluid Mechanics* 159, 50-63.
- Afonso, A. M., M. A. Alves and F. T. Pinho (2011). Electro-osmotic flow of viscoelastic fluids in microchannels under asymmetric zeta potentials. *Journal of Engineering Mathematics* 71, 15-30.
- Afonso, A. M., F. T. Pinho and M. A. Alves (2012). Electro-osmosis of viscoelastic fluids and prediction of electro-elastic flow instabilities in a cross slot using a finite-volume method. *Journal of Non-Newtonian Fluid Mechanics* 179-180, 55-68.
- Babaie, A., A. Sadeghi and M. H. Saidi (2011). Combined electroosmotically and pressure driven flow of power-law fluids in a slit microchannel. *Journal of Non-Newtonian Fluid Mechanics* 166, 792-798.
- Berli, C. L. A. and M. L. Olivares (2008). Electrokinetic flow of non-Newtonian fluids in microchannels. *Journal of Colloid and Interface Science* 320, 582-589.
- Bharti, R. P., D. J. E. Harvie and M. R. Davidson (2009). Electroviscous effects in steady fully developed flow of a power-law liquid through a cylindrical microchannel. *International Journal of Heat and Fluid Flow* 30, 804-811.
- Davidson, M. R., R. P. Bharti and D. J. E. Harvie (2010). Electroviscous effects in a Carreau liquid flowing through a cylindrical microfluidic contraction. *Chemical Engineering Science* 65, 6259-6269.
- Hadigol, M., R. Nosrati and M. Raisee (2011). Numerical analysis of mixed electroosmotic/pressure driven flow of power-law fluids in micro-channels and micro-pumps. *Colloids and Surfaces A* 374, 142-153.
- Huang, H. F. and C. H. Yao (2014). Electrokinetic diffusioosmosis of viscoelastic Phan-Thien-Tanner liquids in slit microchannels. *Journal of Non-Newtonian Fluid Mechanics* 206, 1-10.
- Hussain, M. A., S. Kar and R. R. Puniyani (1999). Relationship between power law coefficients and major blood constituents affecting the whole blood viscosity. *Journal of Biosciences* 24(3), 329-337.
- Jian, Y., L. Yang and Q. Liu (2010). Time periodic electro-osmotic flow through a microannulus. *Physics of Fluids* 22, 042001.
- Kandlikar, S., S. Garimella, D. Li, S. Colin and M. King (2014). *Heat transfer and fluid flow in minichannels and microchannels*. Oxford, Elsevier.
- Karniadakis, G., A. Beskok, N. Aluru (2005). *Micro flows and nano flows: fundamentals and simulation*. New York, Springer.
- Kuznetsov, V. V., O. V. Vitovsky and O. A. Gasenko (2009). Methane steam reforming in an annular microchannel with Rh/Al₂O₃ catalyst. *Journal of Engineering Thermophysics* 18, 187-196.
- Ng, C. O. and C. Qi (2013). Electroosmotic flow of a viscoplastic material through a slit channel with walls of arbitrary zeta potential. *Physics of Fluids* 25, 103102.
- Ng, C. O. (2013). Combined pressure-driven and electroosmotic flow of Casson fluid through a slit microchannel. *Journal of Non-Newtonian Fluid Mechanics* 198, 1-9.
- Nouri-Borujerdi, A. and M. Layeghi (2005). A review of concentric annular heat pipes. *Heat Transfer Engineering* 26, 45-58.
- Park, H. M. and W. M. Lee (2008). Effect of viscoelasticity on the flow pattern and the volumetric flow rate in electroosmotic flows through a microchannel. *Lab on a Chip* 8, 1163-1170.
- Probstein, R. F. (1994), *Physicochemical Hydrodynamics*, New York, Wiley.
- Scampavia, L. D., G. Blankenstein, J. Ruzicka and G. D. Christian (1995). A coaxial jet mixer for rapid kinetic analysis in flow injection and flow injection cytometry. *Analytical Chemistry* 67, 2743-2749.
- Tang, G. H., X. F. Li, Y. L. He and W. Q. Tao (2009). Electroosmotic flow of non-Newtonian fluid in microchannels. *Journal of Non-Newtonian Fluid Mechanics* 157, 133-137.
- Tsao, H. K. (2000). Electroosmotic flow through an annulus. *Journal of Colloid and Interface Science* 225, 247-250.
- Vasu, N. and S. De (2010). Electroosmotic flow of power-law fluids at high zeta potentials. *Colloids and Surfaces A* 368, 44-52.
- Westheimer, D. T. and G. P. Bud Peterson (2001). Visualization of flow boiling in an annular heat exchanger under microgravity conditions. *Journal of Thermophysics and Heat Transfer* 15, 333-339.
- Yang, R. J., L. M. Fu and C. C. Hwang (2001). Electroosmotic entry flow in a microchannel. *Journal of Colloid and Interface Science* 244, 173-179.
- Zhao, C., E. Zholkovskij, J. H. Masliyah and C. Yang (2008). Analysis of electroosmotic flow of power-law fluids in a slit microchannel. *Journal of Colloid and Interface Science* 326, 503-510.

A. Hamed *et al.* / *JAFM*, Vol. 9, No. 1, pp. 367-378, 2016.

Zhao, C. and C. Yang (2011). *Electro-osmotic mobility of non-Newtonian fluids*. *Biomicrofluidics* 5, 014110.

pressure-driven electrokinetic flow of power-law fluids through a rectangular microchannel. *Journal of Non-Newtonian Fluid Mechanics* 203, 38-50.

Zhu, Q., S. Deng and Y. Chen (2014). Periodical